



This is a repository copy of *Spectropolarimetry of the thermonuclear supernova SN 2021rhu: high calcium polarization 79 Days after peak luminosity*.

White Rose Research Online URL for this paper:

<https://eprints.whiterose.ac.uk/192807/>

Version: Published Version

Article:

Yang, Y., Yan, H., Wang, L. et al. (19 more authors) (2022) Spectropolarimetry of the thermonuclear supernova SN 2021rhu: high calcium polarization 79 Days after peak luminosity. *The Astrophysical Journal*, 939 (1). 18. ISSN 1538-4357

<https://doi.org/10.3847/1538-4357/ac8d5f>

Reuse

This article is distributed under the terms of the Creative Commons Attribution (CC BY) licence. This licence allows you to distribute, remix, tweak, and build upon the work, even commercially, as long as you credit the authors for the original work. More information and the full terms of the licence here:

<https://creativecommons.org/licenses/>

Takedown

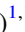




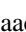













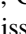

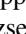
If you consider content in White Rose Research Online to be in breach of UK law, please notify us by emailing eprints@whiterose.ac.uk including the URL of the record and the reason for the withdrawal request.



eprints@whiterose.ac.uk
<https://eprints.whiterose.ac.uk/>



Spectropolarimetry of the Thermonuclear Supernova SN 2021rhu: High Calcium Polarization 79 Days after Peak Luminosity

Yi Yang (杨轶)^{1,19} , Huirong Yan^{2,3} , Lifan Wang⁴ , J. Craig Wheeler⁵ , Dietrich Baade⁶ , Howard Isaacson¹ , Aleksandar Cikota⁷ , Justyn R. Maund⁸ , Peter Hoeflich⁹ , Ferdinando Patat⁷ , Steven Giacalone¹⁰ , Malena Rice^{11,20} , Dakotah B. Tyler¹² , Divya Mishra⁷ , Chris Ashall¹³ , Thomas G. Brink¹ , Alexei V. Filippenko¹ , Lfús Galbany^{14,15} , Kishore C. Patra^{1,21} , Melissa Shahbandeh¹⁰ , Sergiy S. Vasylyev^{1,22} , and Jozsef Vinkó^{6,16,17,18} 

¹ Department of Astronomy, University of California, Berkeley, CA 94720-3411, USA; yyiyangtamu@gmail.com

² Deutsches Elektronen-Synchrotron (DESY), Platanenallee 6, D-15738 Zeuthen, Germany

³ Institut für Physik und Astronomie, Universität Potsdam, Haus 28, Karl-Liebknecht-Str. 24/25, D-14476 Potsdam, Germany

⁴ George P. and Cynthia Woods Mitchell Institute for Fundamental Physics & Astronomy, Texas A&M University, 4242 TAMU, College Station, TX 77843, USA

⁵ Department of Astronomy, University of Texas, 2515 Speedway, Stop C1400, Austin, TX 78712-1205, USA

⁶ European Organisation for Astronomical Research in the Southern Hemisphere (ESO), Karl-Schwarzschild-Str. 2, D-85748 Garching b. München, Germany

⁷ European Organisation for Astronomical Research in the Southern Hemisphere (ESO), Alonso de Cordova 3107, Vitacura, Casilla 19001, Santiago de Chile, Chile

⁸ Department of Physics and Astronomy, University of Sheffield, Hicks Building, Hounsfield Road, Sheffield S3 7RH, UK

⁹ Department of Physics, Florida State University, Tallahassee, FL 32306-4350, USA

¹⁰ Department of Astronomy, University of California Berkeley, Berkeley, CA 94720-3411, USA

¹¹ Department of Astronomy, Yale University, New Haven, CT 06511, USA

¹² Department of Physics & Astronomy, University of California, Los Angeles, CA 90095, USA

¹³ Institute for Astronomy, University of Hawai'i at Manoa, 2680 Woodlawn Drive, Honolulu, HI 96822, USA

¹⁴ Institute of Space Sciences (ICE, CSIC), Campus UAB, Carrer de Can Magrans, s/n, E-08193 Barcelona, Spain

¹⁵ Institut d'Estudis Espacials de Catalunya (IEEC), E-08034 Barcelona, Spain

¹⁶ Konkoly Observatory, CSFK, Konkoly-Thege M. út 15-17, Budapest, 1121, Hungary

¹⁷ ELTE Eötvös Loránd University, Institute of Physics, Pázmány Péter sétány 1/A, Budapest, 1117 Hungary

¹⁸ Department of Optics & Quantum Electronics, University of Szeged, Dóm tér 9, Szeged, 6720, Hungary

Received 2022 May 24; revised 2022 August 13; accepted 2022 August 26; published 2022 October 27

Abstract

We report spectropolarimetric observations of the Type Ia supernova (SN) SN 2021rhu at four epochs: -7 , $+0$, $+36$, and $+79$ days relative to its B -band maximum luminosity. A wavelength-dependent continuum polarization peaking at $3890 \pm 93 \text{ \AA}$ and reaching a level of $p_{\text{max}} = 1.78\% \pm 0.02\%$ was found. The peak of the polarization curve is bluer than is typical in the Milky Way, indicating a larger proportion of small dust grains along the sight line to the SN. After removing the interstellar polarization, we found a pronounced increase of the polarization in the Ca II near-infrared triplet, from $\sim 0.3\%$ at day -7 to $\sim 2.5\%$ at day $+79$. No temporal evolution in high-resolution flux spectra across the Na I D and Ca II H and K features was seen from days $+39$ to $+74$, indicating that the late-time increase in polarization is intrinsic to the SN as opposed to being caused by scattering of SN photons in circumstellar or interstellar matter. We suggest that an explanation for the late-time rise of the Ca II near-infrared triplet polarization may be the alignment of calcium atoms in a weak magnetic field through optical excitation/pumping by anisotropic radiation from the SN.

Unified Astronomy Thesaurus concepts: [Supernovae \(1668\)](#); [Spectropolarimetry \(1973\)](#)

1. Introduction

The mechanism that destroys carbon/oxygen white dwarfs (CO WDs) in binary or multiple systems and produces Type Ia supernovae (SNe) remains uncertain. A key to the distinction between various possible explosion models is offered by measuring the explosion geometry through spectropolarimetry (see Howell et al. 2001, and the review by Wang & Wheeler 2008). The continuum polarization observed in normal Type Ia SNe is generally low within weeks after the SN explosion, for instance, $p \lesssim 0.2\%$ from about 2 weeks before

(SN 2018gv; Yang et al. 2020) to 6 weeks after (SN 2001el, Kasen et al. 2003; Wang et al. 2003; SN 2006X, Patat et al. 2009) the peak of the optical light-curve maximum. This implies high overall spherical symmetry for Type Ia SNe. For example, when seen equator-on, an oblate ellipsoid would have an axis ratio of $\lesssim 1.1$ (Höflich 1991). In contrast, certain prominent spectral lines, such as Si II and Ca II, usually show higher degrees of polarization, within weeks after the SN explosion (Wang & Wheeler 2008; Cikota et al. 2019). This line polarization can be understood as the effect of clumps of chemically distinguished material partially blocking the underlying photosphere. The uneven distribution of the corresponding line opacity leads to an incomplete cancellation of electric (E) vectors over the range of the absorption wavelength, and hence a net line polarization.

Ignition of an exploding WD can, in principle, be in the center, off-center, or throughout the volume of the WD; in addition, it may occur at a single knot, within a confined region, or at multiple locations in the WD (see overviews by Alsabti & Murdin 2017). Different explosion mechanisms can shape distinct explosion geometries and the distributions of

¹⁹ Bengier-Winslow-Robertson Postdoctoral Fellow.

²⁰ NSF Graduate Research Fellow.

²¹ Nagaraj-Noll-Otellini Graduate Fellow.

²² Steven Nelson Graduate Fellow.



various elements that affect the line polarization. Here we summarize some scenarios to account for typical Type Ia SNe that are discussed in the literature.

(i) Deflagration-to-detonation transition may be caused by turbulence in the flame front (delayed-detonation models; Khokhlov 1991a) or strong pulsations of the WD (pulsational delayed-detonation models; Khokhlov 1991b; Khokhlov et al. 1993; Höflich et al. 1996; Plewa et al. 2004; Jordan et al. 2008, 2012; Bravo et al. 2009; Bravo & García-Senz 2009). The abundance distribution of the burning products in the deflagration phase is likely to be mixed sufficiently to produce a high degree of homogeneity in the density distribution. Only the most prominent features, such as Si II and Ca II, are expected to show polarization (of $\lesssim 1\%$). The amplitude of line polarization may depend on the manner in which the ignition is initiated (Seitenzahl et al. 2013; Bulla et al. 2016a). (ii) Dynamical mergers between two WDs (see, e.g., Iben & Tutukov 1984; Webbink 1984; Pakmor et al. 2010) will show significant asymmetry in all abundances and in the density distribution, resulting in a wealth of significantly polarized lines ($\sim 1\%$) across the optical spectrum (Pakmor et al. 2012; Bulla et al. 2016b). (iii) Head-on collision of the WDs may exhibit bimodal chemical distributions including two distinct ^{56}Ni regions (Dong et al. 2015) and significant polarization due to strong departure from spherical symmetry. (iv) WDs with a helium shell may explode with mass below the Chandrasekhar mass (M_{Ch}) limit (Taam 1980; Fink et al. 2010). In this picture, a detonation in the helium layer will send a shock wave inward, triggering a second, off-center detonation in the inner C/O core (Shen et al. 2010). Two-dimensional (2D) and three-dimensional (3D) hydrodynamic simulations suggest that an off-center detonation of the WD causes the core to be more compressed in one direction, thus producing an aspherical distribution of the intermediate-mass elements (IMEs; Bulla et al. 2016a; Boos et al. 2021) and significant line polarization.

Multidimensional hydrodynamic computations of the polarization of a variety of models of Type Ia SNe were conducted for the phase between -10 and $+30$ days relative to peak luminosity by Bulla et al. (2016a, 2016b). During this phase, the photosphere recedes into the layers of IMEs produced in the outer regions of typical explosion models. Line polarization of IMEs such as Si II and Ca II is associated with absorption features and thus traces the deviation from spherical symmetry of the corresponding elements (Höflich 1991; Wang & Wheeler 2008). The photosphere continues to recede over time. After ~ 2 months, most lines and the majority of the continuum flux come from the inner, Fe-rich ejecta. The polarization properties and the chemical distribution of the inner regions could potentially be inferred from nebular-phase spectropolarimetry; however, such data sets are very rare.

Here we report spectropolarimetric observations of the Type Ia SN 2021rhu between -7 and $+79$ days relative to the time of B -band maximum light. Two epochs of high-resolution flux spectra obtained at days $+39$ and $+74$ in order to search for any circumstellar matter (CSM) around the SN will also be discussed. SN 2021rhu was discovered on 2021 July 1 (UT dates are used throughout this paper; Munoz-Arancibia et al. 2021) in the alert stream of the Zwicky Transient Facility (Bellm et al. 2019; Graham et al. 2019) in the edge-on spiral galaxy NGC 7814 and has been classified as a Type Ia SN (Atapin et al. 2021). The photometric and spectroscopic properties of SN 2021rhu are similar to those of normal and

transitional Type Ia SNe (Dhawan et al. 2022). A detailed study of the observational properties of SN 2021rhu will be presented by K. C. Patra et al. (2022, in preparation).

2. Observations and Data Reduction

2.1. VLT FORS2 Spectropolarimetry

Spectropolarimetry of SN 2021rhu was conducted with the Focal Reducer and low-dispersion Spectrograph 2 (FORS2; Appenzeller et al. 1998) on UT1 (Antu) of the ESO Very Large Telescope (VLT) in the Polarimetric Multi-Object Spectroscopy (PMOS) mode. With a $1''$ -wide slit, the spectral resolving power was $R \approx 440$ (or 13 \AA , FWHM) at the center of the wavelength range from ~ 3500 to 9200 \AA . An additional observation on day $+0$ employed the 1200R grism with $R \approx 2140$ (corresponding to $\sim 3 \text{ \AA}$ FWHM around the Si II $\lambda 6355$ feature; see, e.g., Anderson 2018). In order to maximize the blue wavelength coverage, we decided not to use an order-sorting filter (the standard is GG435 with a cut-on wavelength of 4350 \AA). The contamination by second-order light, which starts beyond two times the atmospheric cutoff (i.e., $2 \times 3300 \text{ \AA}$), has an almost negligible effect on the extraction of the true polarization signal at the red end, unless the source is very blue (see the Appendix of Patat et al. 2010). Observations at early phases indicate that the photometric and spectroscopic behavior of SN 2021rhu resembles that of normal Type Ia SNe (Munoz-Arancibia et al. 2021; Atapin et al. 2021), so the SN was not very blue. Table 1 assembles a log of the VLT observations and the extracted polarization properties of SN 2021rhu, as discussed in Section 3.2. Details of the FORS2/PMOS data reduction and the derivation of the Stokes parameters including a debias procedure of the degree of linear polarization introduced by Wang et al. (1997) can be found in the FORS2 Spectropolarimetry Cookbook and Reflex Tutorial,²³ in Cikota et al. (2017), and in Appendix A of Yang et al. (2020), following the procedures of Patat & Romaniello (2006) and Maund et al. (2007).

Below $\sim 4000 \text{ \AA}$, the sensitivity of the VLT FORS2 instrument decreases rapidly. Therefore, flux calibration and estimation of the polarization error at the very blue end of the optical spectrum may suffer from systematic uncertainties, and the polarization features become hard to characterize.

2.2. Keck HIRES Spectroscopy

We obtained two sets of spectra of SN 2021rhu with the High-Resolution Echelle Spectrometer (HIRES; Vogt et al. 1994) instrument on the Keck I 10 m telescope on 2021-8-23 (day $+39$) and 2021-9-27 (day $+74$). We used the C2 decker setup ($14'' \times 0''861$, $R = 45,000$) and integrated for $3 \times 900 \text{ s}$ and $2 \times 1800 \text{ s}$, respectively, at the two epochs. The spectra were reduced following a standard routine of the California Planet Search project (Howard et al. 2010). We corrected the velocity zero-point of the spectral orders containing the Na I D and Ca II H and K lines to the rest frame using the recession velocity of $v_{\text{res}} = 1049 \text{ km s}^{-1}$ measured for the spiral host galaxy NGC 7814 (van Driel et al. 2016) and the barycentric velocity determined following Wright & Eastman (2014) for the UTC at each HIRES observation.

²³ <ftp.eso.org/pub/dfs/pipelines/instruments/fors/fors-pmos-reflex-tutorial-1.3.pdf>

Table 1
VLT Spectropolarimetric Observations of SN 2021rhu

#	Date (UT) / Phase ^a (days)	Exp. Time ^b (s)	Grism / Res. Power	q^{Cont} (%)	u^{Cont} (%)	α (%) β	θ_d (deg)	$\alpha^{\text{Ca II NIR3}}$ (%) $\beta^{\text{Ca II NIR3}}$	$\theta_d^{\text{Ca II NIR3}}$ (deg)	$p_{\text{max}}^{\text{Ca II NIR3}}$ (%)
1	2021-7-8 / -7	$2 \times 4 \times 150$	300V/440	0.04 ± 0.12	0.01 ± 0.11	0.00322 ± 0.00391 0.166 ± 0.040	$184.7_{-1.1}^{+1.1}$	0.0795 ± 0.0765 -1.194 ± 0.885	$155.0_{-7.1}^{+16.4}$	0.30 ± 0.06
2	2021-7-15 /+0	$2 \times 4 \times 80$	300V/440	0.00 ± 0.12	0.00 ± 0.11	$9.60 \times 10^{-5} \pm 0.00354$ -0.0107 ± 0.0439	$179.7_{-1.3}^{+1.3}$	0.138 ± 0.029 -0.951 ± 0.238	$158.2_{-3.2}^{+4.0}$	0.44 ± 0.08
2 ^c	2021-07-15	$2 \times 4 \times 160$	1200R/2140			N.A.	N.A.	N.A.	N.A.	N.A.
3	2021-8- 20 /+36	$2 \times 4 \times 450$	300V/440	-0.03 ± 0.12	0.00 ± 0.12	0.00894 ± 0.00516 0.441 ± 0.063	$191.9_{-1.6}^{+1.5}$	-0.0817 ± 0.0891 1.412 ± 0.430	$207.3_{-5.1}^{+3.4}$	0.82 ± 0.11
4	2021-10-2 / +79	$2 \times 4 \times 300$	300V/440	-0.11 ± 0.38	0.14 ± 0.41	N.A. N.A.	N.A.	-1.664 ± 7.104 1.412 ± 0.430	$222.2_{-25.6}^{+1.3}$	2.48 ± 0.31

Notes.

^a Relative to the estimated peak on UT 2021-7-15/MJD 59410.

^b Each set of observation consists of 2 [loops] \times 4 [half-wave plate angles] \times [time of integration].

^c A higher spectral resolution and a narrower wavelength range of 5700–7100 Å are offered by the grism 1200R.

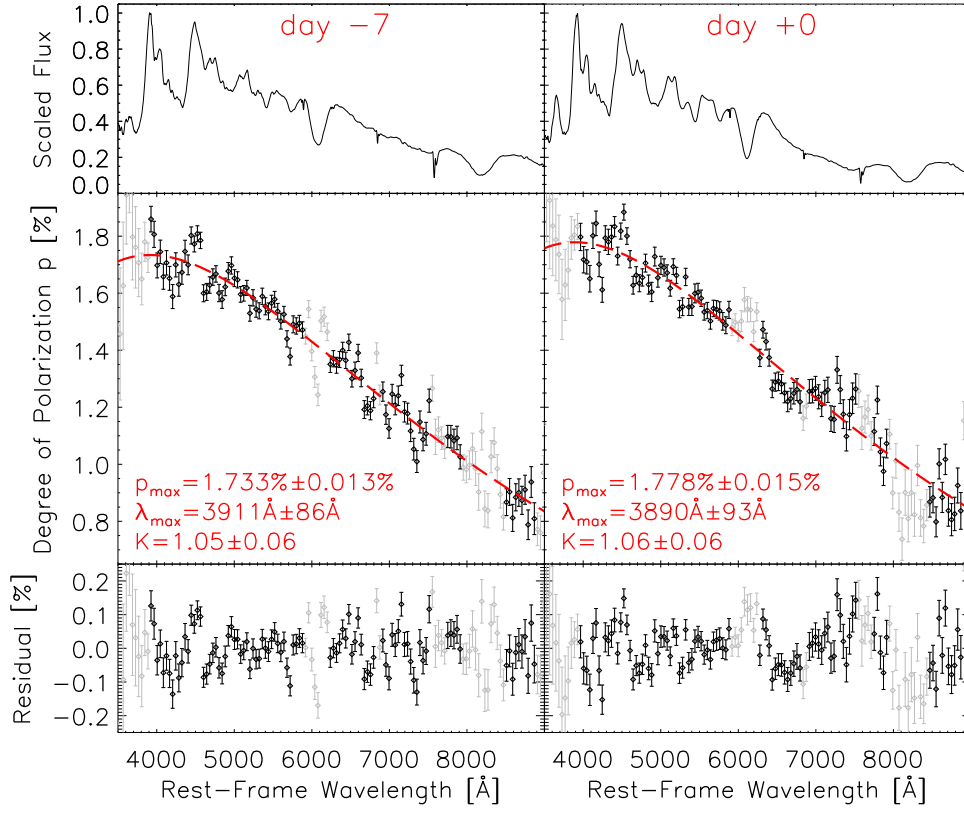


Figure 1. Estimation of the ISP toward SN 2021rhu based on the observations on days -7 (left column) and $+0$ (right column). The top row gives the flux spectra normalized to the maximum value within the range. The middle row presents the degree of linear polarization for the given epochs. The red long-dashed curve indicates the best fit using a Serkowski law. The fitted parameters are labeled in each panel. The data have been rebinned to 40 \AA . Data points plotted in gray were excluded from the fitting since they cover broad and polarized features or major telluric lines. The bottom row shows the residuals from the fit.

3. Results

3.1. Interstellar Polarization

At all epochs, the polarization measured toward SN 2021rhu exhibits a clear wavelength dependence (see the middle panels of Figure 1). In the optical/near-infrared domain, the wavelength (λ) dependence of the interstellar polarization (ISP) can be approximated by the Serkowski law (Serkowski et al. 1975),

$$p(\lambda)/p(\lambda_{\max}) = \exp[-K \ln^2(\lambda_{\max}/\lambda)], \quad (1)$$

where λ_{\max} and $p(\lambda_{\max})$ denote the wavelength and the level of the maximum polarization, respectively. The parameter K describes the width of the ISP peak. For the purpose of estimating the ISP, we exploit the fact that the intrinsic continuum polarization of Type Ia SNe is generally negligible (i.e., $\lesssim 0.2\% - 0.3\%$; Wang & Wheeler 2008). Hence, we fitted Serkowski’s law to the polarization spectra of SN 2021rhu at days -7 and $+0$, and we present the results in Figure 1. Data points near the blue end of the spectra or belonging to the prominent and polarized Si II $\lambda 6355$ and Ca II near-infrared triplet (NIR3) features were excluded in the fitting process. We take the Ca II NIR3 feature to have a rest wavelength of $\lambda_{0,\text{Ca}} = 8570 \text{ \AA}$, averaged over the wavelengths of the triplets (8500.36 \AA , 8544.44 \AA , and 8664.52 \AA). The fitted ISP curve for day $+0$ ($K = 1.06 \pm 0.06$, $\lambda_{\max} = 3890 \pm 93 \text{ \AA}$, and $p(\lambda_{\max}) = 1.778\% \pm 0.015\%$) has been adopted for the ISP corrections throughout the paper. The parameters are consistent with the

values determined based on observations at day -7 (see the left panels of Figure 1), thus confirming the assumption of constant low continuum polarization of SN 2021rhu around its peak luminosity. The actual fitting and correction process has been carried out separately for the Stokes parameters Q and U to obtain their values intrinsic to the SN at all observed phases. We also fitted the ISP by adding a secondary component that characterizes any contribution from the Galactic dust. A Galactic reddening component can be estimated as $E(B - V)^{\text{MW}} = 0.04 \text{ mag}$ based on Schlafly & Finkbeiner (2011) and Cardelli et al. (1989). This provides an upper limit on the polarization by the Milky Way dust induced by dichroic extinction: $p_{\text{ISP}} < 9\% \times E(B - V)$ (Serkowski et al. 1975), and $p_{\max}^{\text{MW}} \leq 0.36\%$. Adopting a fixed $K^{\text{MW}} = 1.15$ (Serkowski et al. 1975), we found that p_{\max}^{MW} is consistent with zero, suggesting that the observed ISP toward SN 2021rhu is mainly contributed by its host.

3.2. Intrinsic Polarization of SN 2021rhu

In Figures 2–5 we present the ISP-corrected spectra of Stokes parameters, degree of polarization, and polarization position angle obtained at four epochs from days -7 to $+79$. The figures cover a wavelength range $3600 - 9150 \text{ \AA}$, and the data have been rebinned to 40 \AA in order to increase the signal-to-noise ratio but also make sure that major broad spectral features are sampled by at least $\sim 5 - 10$ resolution elements. The polarization position angle in panel (e) is presented without subtracting the ISP since $\text{PA} = (1/2)\tan^{-1}(U/Q)$ will display random values when Q is low after a baseline ISP has been

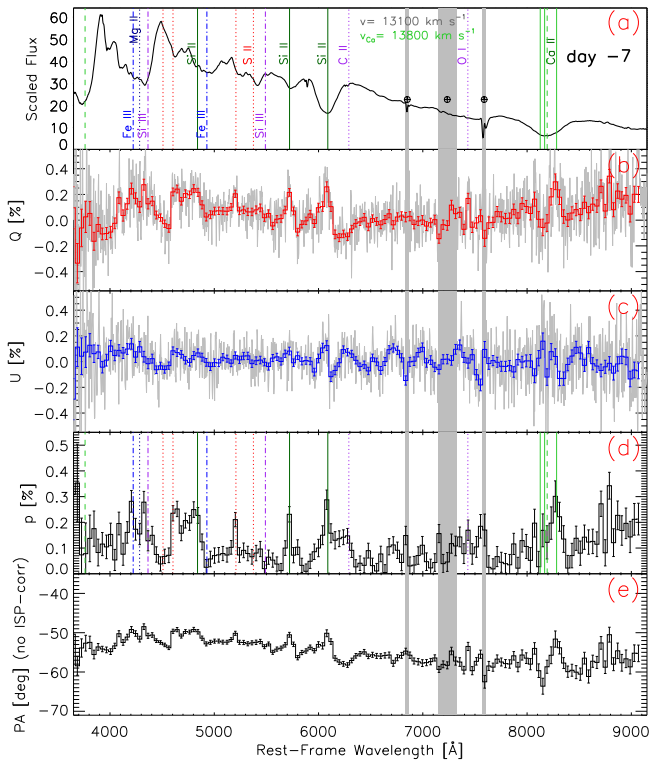


Figure 2. Spectropolarimetry of SN 2021rhu observed on day -7 . The five panels (from top to bottom) present (a) the scaled flux spectrum; (b, c) the normalized Stokes parameters Q and U , respectively; (d) the polarization spectrum (p); and (e) the polarization position angle (PA). The diagrams in panels (b)–(d) represent the polarization after ISP correction. PAs in panel (e) are presented before subtracting the ISP. The data have been rebinned to 40 \AA , while the Stokes Q and U parameters approximately sampled with the detector pixel size are indicated by gray histograms in panels (b)–(c).

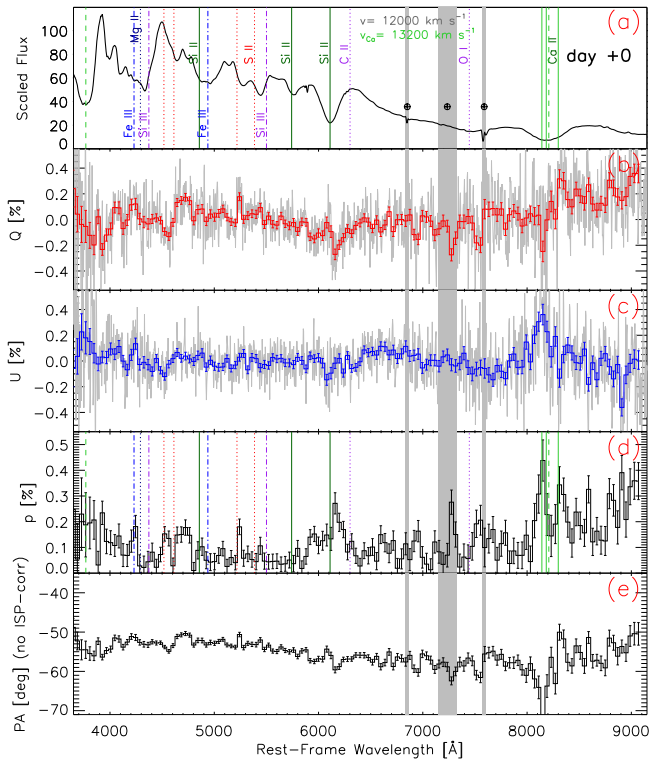


Figure 3. Same as Figure 2, but for day $+0$.

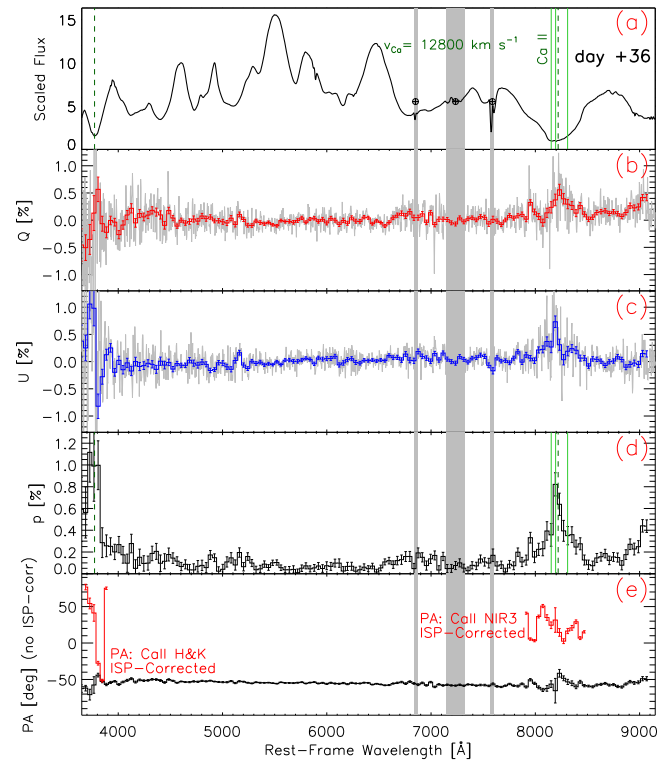


Figure 4. Same as Figure 2, but for day $+36$. The red histograms in panel (e) display the ISP-corrected PA across Ca II H and K and Ca II NIR3 after correction for the ISP.

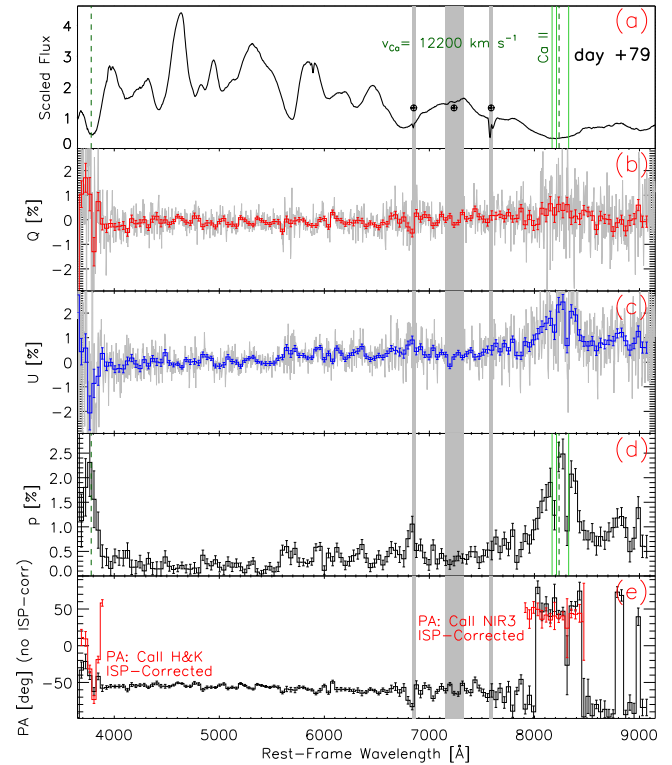


Figure 5. Same as Figure 2, but for day $+79$. The red histograms in panel (e) display the ISP-corrected PA across Ca II H and K and Ca II NIR3 after correction for the ISP.

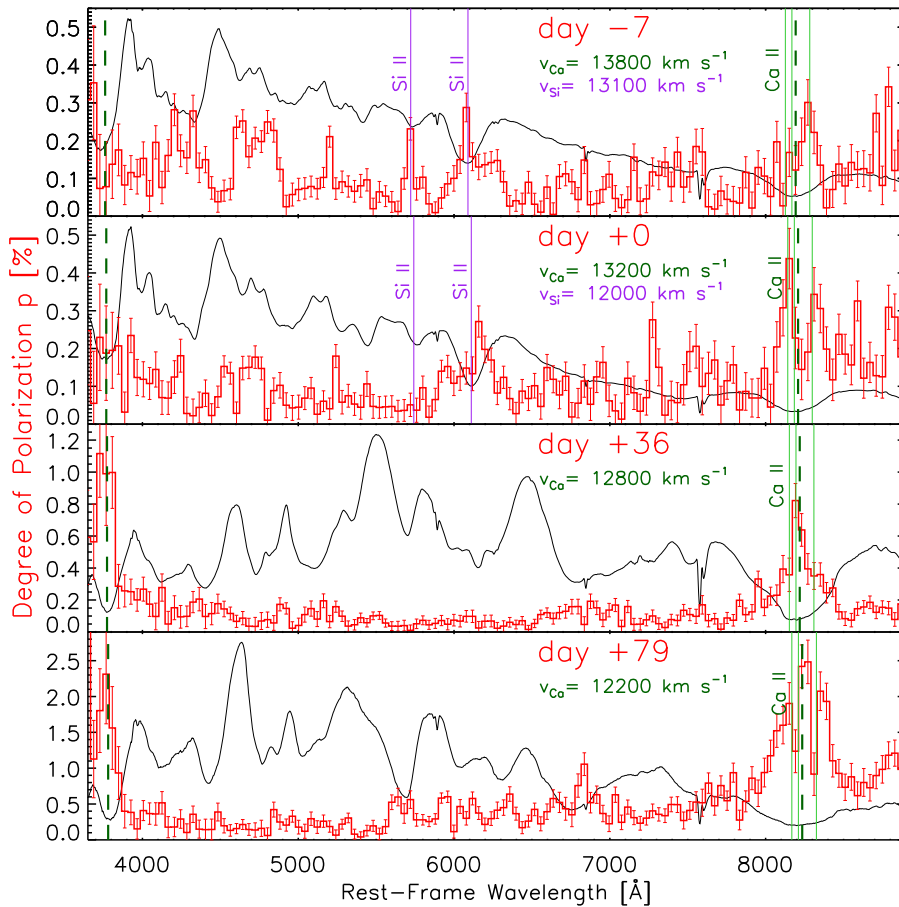


Figure 6. Evolution of the intrinsic polarization of SN 2021rhu. For each epoch, the degree of polarization is presented (red histogram) with 40 Å binning, together with the full-resolution and arbitrarily scaled flux spectrum (black line). Ca II NIR3 features at all epochs are labeled with their velocities (v_{Ca}) calculated with $\lambda_{0,\text{Ca}} = 8570$ Å (Section 3.1). Vertical light-green lines indicate the locations of the three components of Ca II NIR3. The two vertical green dashed lines trace the evolution of the Ca II H and K and the Ca II NIR3 velocities. Vertical purple lines identify the Si II $\lambda 5976$ and Si II $\lambda 6355$ features at days -7 and $+0$. The Ca and Si velocities were determined from the absorption minima corresponding to $\lambda_{0,\text{Ca}}$ and Si II $\lambda 6355$, respectively. The degree of polarization across both Ca II NIR3 and Ca II H and K shows a substantial increase at later epochs.

removed. The error bars in the histograms that provide the polarization measurements represent the 1σ uncertainty.

The temporal evolution of the degree of polarization of SN 2021rhu after the ISP correction is shown in Figure 6. We also estimate the continuum polarization based on the Stokes parameters over the wavelength range 5000–6800 Å with the highly polarized Si II lines excluded. The error-weighted mean Stokes parameters (q^{Cont} , u^{Cont}) across this region from days -7 to $+79$ are presented in Table 1. The error has been estimated by adding the statistical uncertainties and the standard deviation calculated from the 40 Å binned spectra within the continuum wavelength range in quadrature. The q^{Cont} and u^{Cont} are consistent with zero within the selected wavelength range, and the level of polarization intrinsic to SN 2021rhu across the optical continuum remains low from days -7 to $+79$. The most noticeable behavior in the spectropolarimetric evolution of SN 2021rhu is the strong increase in the peak polarization of the Ca II lines from days $+36$ to $+79$, namely, in Ca II H and K from $1.1\% \pm 0.3\%$ to $2.3\% \pm 0.7\%$, and in Ca II NIR3 from $0.8\% \pm 0.1\%$ to $2.5\% \pm 0.3\%$ (see Table 1 and Figure 6), as measured in the data with 40 Å bin size. At all epochs, the peak polarization across Ca II NIR3 is significantly higher than in the continuum.

A polarization signal is seen in Si II $\lambda 6355$ on days -7 and $+0$. Thereafter, it vanished in accordance with the

disappearance of the Si II feature from the total-flux spectrum a few weeks past maximum light. This early Si II polarization can be understood as an inhomogeneous obscuration of the photosphere. With the recession of the photosphere into the interior ejecta below the Si-rich layer, the optical depth of the Si becomes small, and polarization by blocking portions of the photosphere cannot occur.

The polarization profiles of the Ca II NIR3 and Si II $\lambda 6355$ lines exhibit rich structures that also evolve with time. For the former complex, we infer the expansion velocity from the absorption minimum of the Ca II NIR3 feature in the total-flux spectrum, namely, $v_{\text{Ca}} = 13,800$, $13,200$, $12,800$, and $12,200$ km s $^{-1}$ at days -7 , $+0$, $+36$, and $+79$, respectively, as shown in Figure 2–6. We also mark the corresponding expansion velocities of the three transitions with green vertical solid lines. The Ca II H and K feature has almost the same velocity as measured from Ca II NIR3, and we also characterize it with v_{Ca} . The velocity of Si II $\lambda 6355$ is also labeled in Figure 2–3 and 6–7, namely, $v = 13,100$ and $12,000$ km s $^{-1}$ at days -7 and $+0$, respectively. Identifications of major spectral lines are provided for days -7 and $+0$, before the SN has entered the nebular phase. All spectral features except for the Ca II lines marked in Figures 2 and 3 are labeled for the photospheric velocity v . Different colors were used to provide a

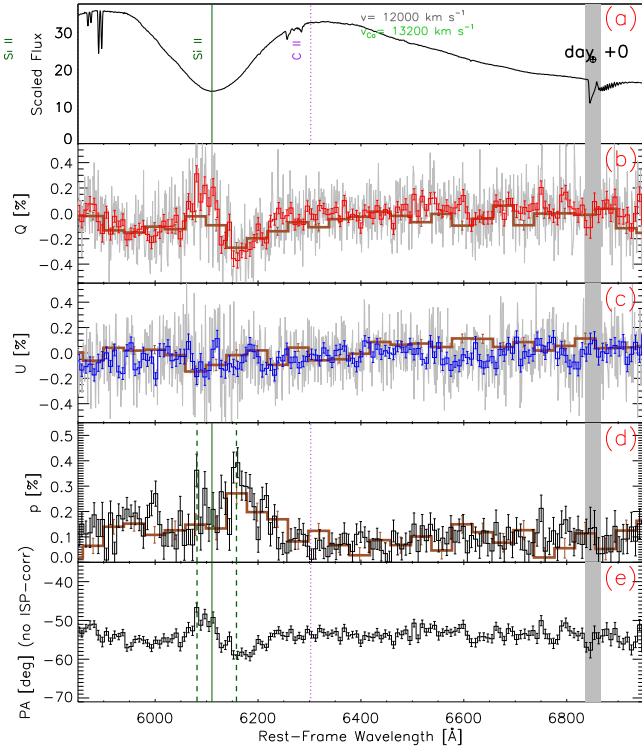


Figure 7. Similar to Figure 2, but for day +0 at higher spectral resolution. The data have been rebinned to 8 \AA . For comparison, low-resolution data obtained at the same epoch rebinned to 40 \AA are shown by the brown thick histograms in panels (b)–(d). The vertical solid green lines in panels (a) and (d) represent the minimum of the total-flux absorption line at $12,000 \text{ km s}^{-1}$. The left and right vertical dashed lines in panel (d) mark the two polarization peaks at $13,500$ and 9600 km s^{-1} , respectively. The gray shaded area identifies a region with a major telluric feature.

better separation of the lines. Major telluric features are marked with gray shaded areas.

At day +0, two peaks appear in the polarization profile of Ca II NIR3, at $\sim 15,400$ and $\sim 8700 \text{ km s}^{-1}$ with respect to the rest frame of SN 2021rhu. They bracket the Ca II NIR3 and Ca II H and K velocities of $\sim 13,200 \text{ km s}^{-1}$ measured at the same epoch. By day +79, three peaks near $15,700$, $11,500$, and 7500 km s^{-1} had developed in the Ca II NIR3 polarization profile. At this epoch, v_{Ca} has decelerated less and appears at $12,200 \text{ km s}^{-1}$. The uncertainty of the stated velocities is dominated by the width of the smallest resolution element, namely, half of 8 \AA for Si II $\lambda 6355$ in the higher-resolution observation and half of 40 \AA for Ca II NIR3, corresponding to ~ 200 and $\sim 700 \text{ km s}^{-1}$, respectively. The uncertainties represent the maximum possible error due to rounding of wavelengths in spectral bins. Inspection of the raw data before spectral rebinning confirms the reality of the structures and of their evolution. From the available data, it is not possible to conclude whether the three polarization peaks correspond to the three triplet components or have a different origin.

At days -7 and $+0$, the expansion velocity of the SN ejecta inferred from the absorption minimum in the Si II $\lambda 6355$ flux profile was $13,100$ and $12,000 \text{ km s}^{-1}$ (marked by the vertical solid and dotted-dashed lines in Figures 2–3 and 6), respectively. The higher-resolution polarization profile of this line from day +0 (this observation does not cover the Ca II NIR3 region) exhibits two peaks. At about $13,500$ and 9600 km s^{-1} , respectively (highlighted by the dashed dark-green lines in Figures 7(d) and (e)), their velocities are different

from that of the absorption minimum. A peak and a trough in Q at the position of Si II $\lambda 6355$ (Figure 7(b)) lead to different position angles (Figure 7(e)). Without ISP subtraction, the polarization position angles of the blue (-50.0 ± 2.5) and the red (-57.5 ± 2.0) components bracket that of the continuum (-53.5 ± 1.3). The position angles of the blue and the red components were estimated by taking the error-weighted mean value in a velocity range of $\pm 800 \text{ km s}^{-1}$ relative to the respective peak. The continuum PA was computed between 6300 and 6700 \AA . In the low-resolution observations on the same date with grism 300V (overplotted in brown in Figures 7(b)–(d)), only traces of the complex polarization structure are visible as some asymmetry. The differences between Si II $\lambda 6355$ and Ca II NIR3 in the structure and evolution of their multiple polarization components will be analyzed by K. C. Patra et al. (2022, in preparation).

3.3. Na I D and Ca II H and K Flux Profiles

Since any CSM will be exposed to intense UV radiation from the SN explosion, embedded elements such as Na and Ca are likely to be ionized. Unlike most of the broad features that arise from the expanding ejecta that retain high kinetic energy, lines from these elements would be narrow enough so that any subcomponents of each feature could be seen separately with higher spectral resolution. Additionally, the Na I D line provides a good tracer of gas and dust, and its strength is correlated with the dust reddening along the line of sight (Munari & Zwitter 1997; Poznanski et al. 2012; Phillips et al. 2013). Temporal variability of such narrow absorption lines would indicate the evolving conditions of the CSM ionization induced by the variable SN radiation field. Therefore, this observational signature has been used to search for CSM around Type Ia SNe (Patat et al. 2007; Simon et al. 2009; Sternberg et al. 2011; Wang et al. 2019).

In order to investigate any temporal evolution of circumstellar Na and Ca line profiles of SN 2021rhu, we approximate the pseudocontinuum by a low-order polynomial fitted to the spectrum between $\sim \pm 20 \text{ \AA}$ of the central wavelength with the absorption line excluded. The flux spectrum spanning each line profile was then divided by the pseudocontinuum spectrum. The line profiles are shown in Figure 8. For SN 2021rhu, we identify no temporal evolution in the Na I D doublet (5895.92 , 5889.95 \AA) and the Ca II H and K doublet (3968.47 , 3933.66 \AA). At both epochs, two complexes of absorption features with centroids at ~ -10 and $\sim +10 \text{ km s}^{-1}$ plus a shallower component at $\sim +60 \text{ km s}^{-1}$ are visible in the lines of Ca II H and K. The Na I D doublet exhibits a broad, saturated profile at almost zero velocity blended with a narrow component near 15 km s^{-1} , plus another narrower component centered at $\sim 52 \text{ km s}^{-1}$. The reddest component displays a slightly higher velocity in Ca II H and K compared to the Na I D doublet. The relatively simple line profiles of SN 2021rhu do not indicate the presence of numerous resolved velocity components that typically span a velocity range of a few hundred kilometers per second as found in some strongly reddened Type Ia SNe (see, e.g., SN 2006X, Patat et al. 2007; SN 2014J, Graham et al. 2015; SN 1999cl, Blondin et al. 2009). SN 2007le exhibited narrow, time-variable Na I D absorption and a moderate amount of reddening ($E(B - V) = 0.27 \text{ mag}$; Simon et al. 2009). The same feature in SN 2021rhu displayed a single component, while a complex absorption profile with approximately seven distinct velocity components

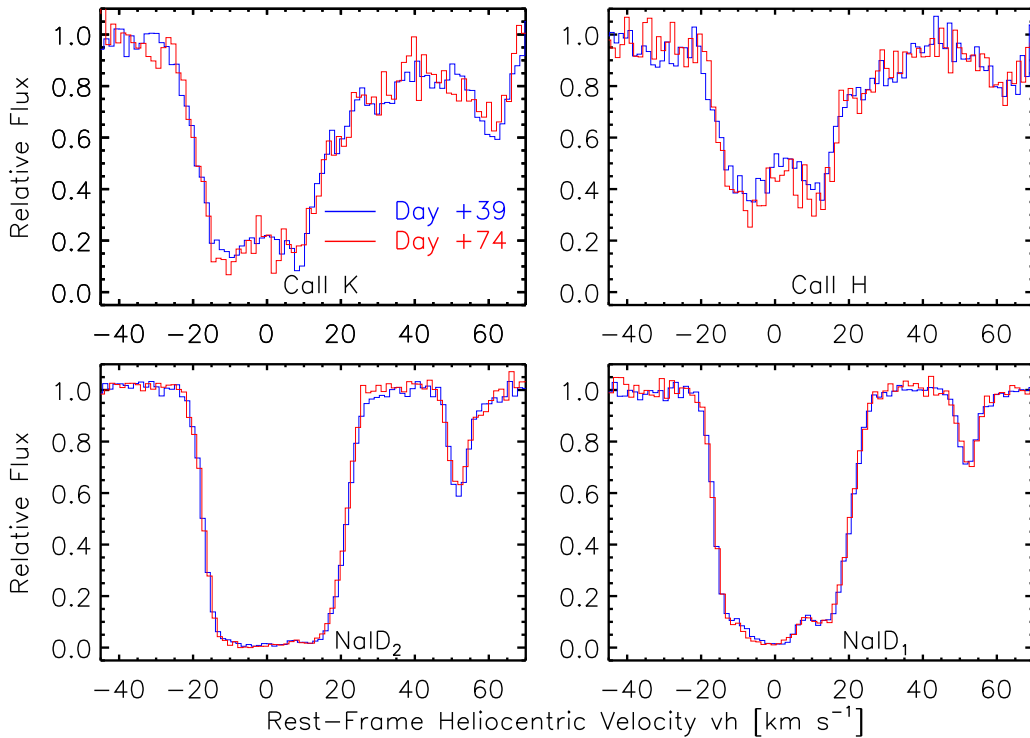


Figure 8. Keck/HIRES spectra of SN 2021rhu in velocity space relative to Ca II K (top left), Ca II H (top right), Na I D₂ (bottom left), and Na I D₁ (bottom right) features. The observed spectra have been divided by the respective ambient pseudocontinuum. No apparent temporal evolution between the two epochs has been identified.

was found in SN 2007le. Most of the Na I and Ca II H and K profiles in SN 2021rhu are confined between ~ -20 and $+60$ km s^{-1} . They most likely arise in a single interstellar dust sheet intersecting the sight line. The lack of temporal evolution suggests constant ionization conditions of the dust cloud exposed to the variable SN radiation field between the observations of HIRES spectroscopy at days +39 and +74. However, the Keck HIRES observations starting from day +39 cannot rule out the possibility that the CSM may have been present at smaller distances to the SN and evaporated by the radiation at early phases. Alternatively, the Na lines were absorbed by the foreground dust grains at large distances. In any case, we infer a rather clean circumstellar environment around day +80 and a large distance between SN 2021rhu and the dust cloud where the interstellar lines form.

4. Discussion

The polarization of SN 2021rhu shows a steep increase from the red to the blue wavelengths and peaked significantly blueward of the galactic average at ≈ 5500 Å (Whittet et al. 1992), i.e., $p_{\text{max}} = 1.78\% \pm 0.02\%$ and $\lambda_{\text{max}} = 3890 \pm 93$ Å. Such a behavior has been seen in some Type Ia SNe that show strong extinction ($E_{B-V}^{\text{host}} \gtrsim 0.5$ mag), but the peak polarization of SN 2021rhu is lower compared to such events, for example, SN 1986G ($p_{\text{max}} = 5.16\% \pm 0.04\%$, $\lambda_{\text{max}} = 4300 \pm 10$ Å; Hough et al. 1987), SN 2006X ($p_{\text{max}} > 8\%$, $\lambda_{\text{max}} \lesssim 4000$ Å; Patat et al. 2009), SN 2008fp ($p_{\text{max}} > 2.2\%$, $\lambda_{\text{max}} \lesssim 4200$ Å; Cox & Patat 2014), and SN 2014J ($p_{\text{max}} > 6.6\%$, $\lambda_{\text{max}} \lesssim 4000$ Å; Kawabata et al. 2014; Patat et al. 2015; Porter et al. 2016; Srivastav et al. 2016; Yang et al. 2018). However, the polarization wavelength dependence of SN 2021rhu is still significantly deviated from the Milky Way average, indicating

an enhanced proportion of small grains along the Earth – SN 2021rhu sight line compared to that in the mean Galactic dust (Whittet et al. 1992; Draine 2003).

After the ISP correction based on the low continuum polarization of Type Ia SNe around peak brightness, major spectral lines of SN 2021rhu show moderate polarization. This behavior is consistent with that generally found for Type Ia SNe. The low continuum polarization at day +79 also suggests the absence of a large amount of CSM within $\sim 2 \times 10^{17}$ cm. This is because the photons scattered by a circumstellar dust cloud can be highly polarized at large scattering angles, causing a significant increase in the continuum polarization (Wang & Wheeler 1996; Yang et al. 2018). In order to produce a net polarized signal via CSM scattering, the CSM distribution on the plane of the sky needs to deviate from point symmetry. Such symmetry would lead to a complete cancellation of the electric vectors (i.e., zero net polarization). SN 2021rhu exhibits a spherical explosion as indicated by the low continuum polarization that is consistent with zero as measured from as early as ~ 7 days before the peak luminosity. Such a high degree of spherical symmetry is inconsistent with the WD – WD merger-induced explosion models, which predict modest ($\gtrsim 0.3$) to strong ($\sim 1\% - 2\%$) continuum polarizations as seen along and perpendicular to the equatorial plane, respectively (Bulla et al. 2016b). The intermediate line polarization observed before and around the peak luminosity of SN 2021rhu and the presence of the small-scale polarization structures across the spectral lines are compatible with the moderate chemical nonuniformity predicted by the delayed-detonation and sub- M_{Ch} helium-shell detonation scenarios (Bulla et al. 2016a). Spectropolarimetry of Type Ia SNe beyond ~ 30 days is still very rare. Our observations of SN 2021rhu offer the first opportunity to follow the temporal evolution, and exploit the

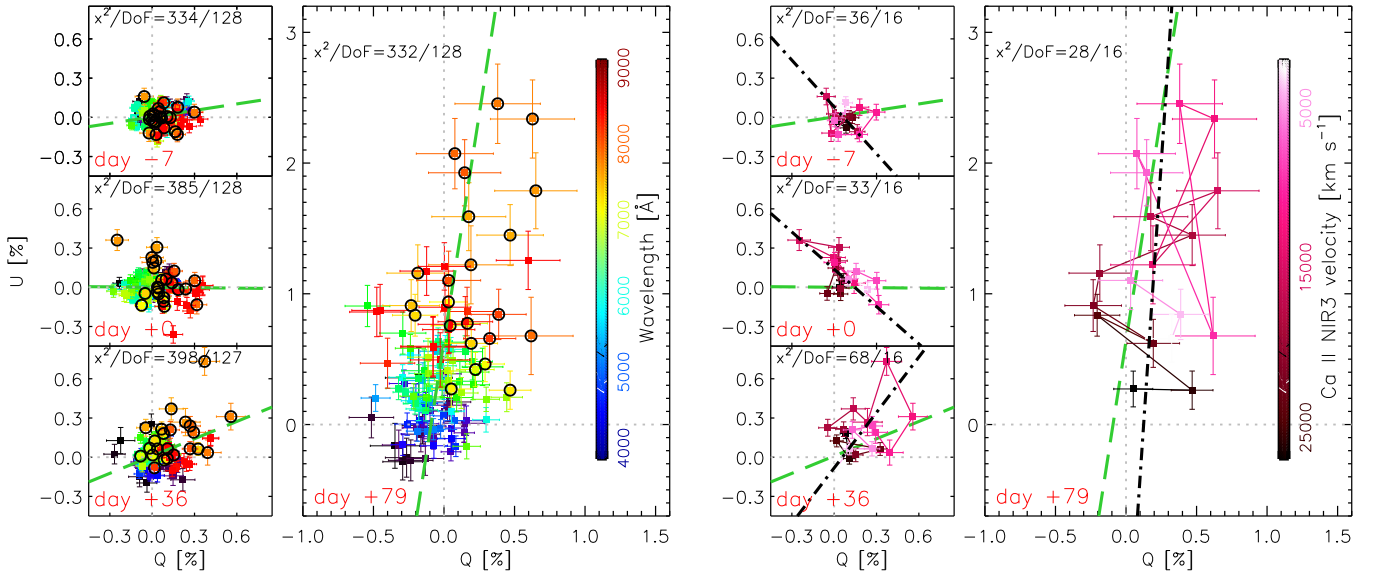


Figure 9. ISP-corrected observations of SN 2021rhu in the Stokes Q – U plane. The data have been rebinned to 40 \AA . The four subpanels on the left (three small square panels for epochs 1–3, plus a larger rectangular panel for epoch 4) present the data in the range 3850 – 9100 \AA , the wavelengths of which are indicated by the left color bar. The ranges of Q and U in the square and rectangular panels are different, but the scales for Q and U are the same in all subpanels. The green long-dashed lines trace the dominant axis of the continuum at different epochs. Note that the dominant axis fitting at day $+79$ does not represent the orientation of the optical ejecta (see Section 4.2). Data points marked with open black circles indicate the spectral region covering the Ca II NIR3 feature. The corresponding four subpanels on the right show the Ca II line over the velocity range $27,000$ – $20,000 \text{ km s}^{-1}$. The right color bar indicates the velocity range of the Ca II NIR3 complex. The light-green long-dashed lines in both left and right subpanels represent the dominant axis fitted to the presented optical wavelength range, while the gray dotted–dashed lines in the right subpanels trace the dominant axis over the Ca II NIR3 feature.

diagnostic power, of the polarization of spectral features at such late epochs.

4.1. Multiple Polarization Components of $\text{Si II } \lambda 6355$

The additional higher-resolution spectropolarimetry obtained around the peak luminosity of SN 2021rhu allows us to determine the geometric signatures left behind by the propagation of the burning front at smaller physical scales, on the order of a few hundred kilometers per second. As shown in Figure 7, the polarization modulation, which is unresolved in the conventional flux spectrum (although the latter has a spectral resolution that is more than an order of magnitude higher), suggests that more than one major line-forming region is present. For comparison, in Figure 7 we also present the Stokes parameters obtained at the same epoch with the low-resolution 300V grism as shown in Figure 3. Such a polarized line complex near the SN light-curve peak has also been reported for SN 2018gv (Yang et al. 2020). The shape of the polarized line profile of SN 2021rhu is not identical to that in SN 2018gv, but both cases may arise from multiple opacity components of clumps and/or shells. Additionally, the small-scale modulations on the order of a few hundred kilometers per second can only be discerned in the spectropolarimetry spectra obtained with the higher-resolution grism 1200R, rather than the low-resolution grism 300V. The comparison between the low- and high-resolution observations also demonstrates the feasibility of resolving small-scale structures in the SN ejecta with high-resolution spectropolarimetry.

In addition to the substructures across the polarization spectrum of the $\text{Si II } \lambda 6355$ at the SN peak luminosity, polarization peaks are also seen across both $\text{Si II } \lambda 6355$ and $\text{Si II } \lambda \lambda 5898, 5979$ absorption features at day -7 . These narrow peaks are no longer distinguishable at day $+0$ (see Figures 2, 3, and 6). The narrow polarization components are

real, and they are also seen under smaller sizes of spectral binning. Their FWHM widths are $\lesssim 1000 \text{ km s}^{-1}$ as measured at day -7 , reflecting the presence of Si-rich clumps with a similar scale in velocity space that intersect the photosphere. At day $+0$, the photosphere recedes into the deeper layers of the ejecta. The disappearance of these narrow polarization peaks and the evolution of the small-scale modulations seen from Figures 3, 6, and 7 can be understood as the retreating photosphere has passed the clumps of Si-line opacities, which produced the narrow polarization peaks at day -7 . Future spectropolarimetric observations with a higher cadence will provide a greater spatial resolution in depth, therefore enabling a more comprehensive tomography of the SN ejecta, and trace the geometric properties of any small-scale structures.

4.2. The Dominant Axes of the Continuum and the Ca II NIR3 Line Polarization

Presenting the spectropolarimetry on the Stokes Q – U plane provides an intuitive layout of the axisymmetry of the continuum and across different spectral features (Wang et al. 2001). For example, an axially symmetric structure will imprint a straight line in the Stokes Q – U plane, the so-called “dominant axis” (Wang et al. 2003; Maund et al. 2010):

$$U = \alpha + \beta Q. \quad (2)$$

After ISP correction, departures from spherical and axial symmetries in the ejecta are indicated in the Q – U diagram by their distances from the origin and deviations from the dominant axis, respectively.

In Figure 9 we present the ISP-corrected Stokes parameters in the Stokes Q – U plane between days -7 and $+79$. The dominant axes of SN 2021rhu were determined by performing an error-weighted linear least-squares fitting to the continuum polarization ($3850 \text{ \AA} \leq \lambda \leq 9100 \text{ \AA}$) and to the Ca II NIR3

feature ($7800 \text{ \AA} \lesssim \lambda \lesssim 8510 \text{ \AA}$, corresponding to a velocity range from $27,000$ to 2000 km s^{-1}), respectively. The fitted dominant axes for SN 2021rhu at different epochs are plotted in Figure 9, and the derived parameters are given in Table 1. Based on the $Q-U$ diagrams in the left panels of Figure 9, the optical ejecta of SN 2021rhu observed in the first three epochs (days -7 to $+36$) are consistent with a dominant axis that rotates with time, while deviations from a single axial symmetry are also notable as indicated by the scatter about the dominant axis reflected by the large values of χ^2 labeled in each subpanel. At day $+79$, the dominant axis fitted to the optical spectrum is mostly defined by the significantly polarized Ca II NIR3 line. After excluding the wavelength range covering the Ca II NIR3 feature (i.e., the black circled data points in the left rectangular panel of Figure 9), the remaining data points are scattered around $(0, 0)$ and do not exhibit any prominent dominant axis. Therefore, we conclude that the optical ejecta do not follow any conspicuous axial symmetry at day $+79$.

The $Q-U$ diagram across the Ca II NIR3 feature exhibits complicated configurations. Loop-like structures can be seen before day $+36$. Such patterns across the Ca II NIR3 line are observed in other typical Type Ia SNe and represent variations in the amplitude and orientation of the polarization as a function of velocity or depth, indicating the deviation from axial symmetry (Wang & Wheeler 2008). At the last epoch at day $+79$ (the large left and right subpanels in Figure 9), the scatter about the dominant axis of the Ca line is smaller, but the complex Ca II NIR3 polarization profile cannot be described by a single loop. Within the framework of a model in which the polarization is produced by line opacity that unevenly blocks the underlying photosphere, the Ca II NIR3 polarization may indicate the presence of multiple Ca-rich components in the inner layers of the ejecta. Although the photosphere of Type Ia SNe may still persist after day ~ 100 as evidenced by the presence of permitted lines (Black et al. 2016), the above interpretation of the presence of multiple Ca-rich components obscuring the SN photosphere will be invalid if, at late phases, the ejecta have become sufficiently optically thin that electron scattering may not be able to produce considerable polarization signals. In Section 4.4, we propose an alternative mechanism of atomic alignment that generates polarized signals not by patchy photospheric electron scattering but through the alignment of atomic angular momentum in an anisotropic radiation field.

4.3. The Late-time Increase in the Polarization of the Ca II Lines

The apparent increasing Ca II NIR3 polarization of SN 2021rhu at days $+36$ and $+79$ has previously only been reported for SN 2006X, which showed an increase from $\sim 0.6\%$ around maximum luminosity to $\sim 1.2\%$ at day $+39$ (Patat et al. 2009). SN 2001el, which is the only other Type Ia SN with Ca II NIR3 polarization measured at a considerable late phase, did not show such polarization signals at day $+41$ (Wang et al. 2003). Although the uncertainty becomes larger near the blue end of the spectral coverage, a similar evolution of Ca II polarization is also seen from the Ca II H and K lines of SN 2021rhu. The nondetection of the Ca II NIR3 polarization in SN 2001el at day $+41$ (Wang et al. 2003) may be due to an orientation effect or an intrinsic diversity among Type Ia SNe. Considering the sparse sample of polarimetry, a meaningful conclusion is not currently feasible.

The evolution of the Ca II NIR3 from $\sim 0.3\%$ at around the peak to $\sim 2.5\%$ at day $+79$ is thus unprecedented. For example, the polarization peak in the Ca II NIR3 profile of Type Ia SNe around maximum light is generally $\lesssim 1\%$ (Wang & Wheeler 2008). By far the only exception, SN 2004dt, displayed a peak Ca II NIR3 polarization of $\sim 0.7\% - 2\%$ (Wang et al. 2006). This high line polarization was observed around the peak luminosity, and it is incompatible with the $\lesssim 0.8\%$ maximum line polarization predicted by hydrodynamic models for 2D double detonation and 3D delayed detonation (Bulla et al. 2016a).

This ‘‘repolarization’’ behavior seen in SN 2006X has been explained in the context of a deflagration/detonation model by a partial blocking of the photosphere when it had receded to within the inner edge of the Ca layer at $8000 - 9000 \text{ km s}^{-1}$ (Patat et al. 2009). Detailed modeling of the degree of asymmetry between the bottom of the Ca layer and the outer parts of the Fe-rich ejecta at later times is necessary to determine whether the Ca II NIR3 polarization of SN 2021rhu at day $+79$ can be accommodated in the context of an M_{Ch} deflagration/detonation picture. This may be a challenge. As the ejecta expand, the optical depth decreases approximately $\propto r(t)^{-2}$ or $\propto t^{-2}$, where $r(t)$ represents the radius reached by freely expanding ejecta at time t after the SN explosion. After a few months, the size of the $\tau = 2/3$ photosphere has substantially decreased. The light emitted by the SN is dominated by numerous overlapping line transitions of Fe-group elements. The abundant overlying narrow lines form a ‘‘quasi-continuum’’ spectrum, superimposed by several strong Fe and Co emissions. The late-time emission-dominated spectra trace the distribution of the Fe-group burning products near the central energy source. These emissions are essentially unpolarized, resulting in an absence of polarized photons to be blocked in the first place. Therefore, the decreasing scattering cross section over time makes the photosphere obscuration mechanism less likely to account for the significant Ca II polarization at late times. Due to the relatively large systematic uncertainties in the very blue end of the optical continuum (Section 2.1), we refrain from an interpretation of the polarization behavior measured across the Ca II H and K lines.

4.4. Considerations Based on Atomic Alignment in a Weak Magnetic Field

We suggest an alternate possibility that might produce the high Ca II polarization as found in SN 2021rhu at day $+79$. This process involves photoexcitation in an anisotropic radiation field when the electron-scattering opacity in the SN ejecta has decreased substantially. The lower levels of Ca II NIR3 are metastable states that can be geometrically aligned through photoexcitation by an anisotropic radiation field. In an interstellar medium that has a weak magnetic field, a subsequent realignment of the angular momentum of the atoms in their ground state may happen through magnetic precession (see, e.g., Happer 1972; Landolfi & Landi Degl’Innocenti 1986). Such a magnetic realignment will take place if the Larmor precession rate, ν_L , is greater than the photoexcitation rate, τ_R^{-1} , from the ground state of the atoms: $\nu_L > \tau_R^{-1}$ (Yan & Lazarian 2006). The atoms’ angular momentum will then be realigned with respect to the magnetic field. In the case of $\nu_L \approx \tau_R^{-1}$, this ‘‘Hanle effect’’ will become effective in a relatively stronger magnetic field (Hanle 1924; Ignace et al. 1997; Yan & Lazarian 2008).

The incident flux must be anisotropic in order to differentially excite the atoms in different magnetic sublevels (see, e.g., Happer 1972; Landolfi & Landi Degl’Innocenti 1986; and the review by Yan & Lazarian 2012). In the presence of anisotropic flux, the angular momentum of the atoms will also be distributed anisotropically. The result is the induction of unequal populations over the magnetic sublevels that correspond to different magnetic quantum numbers, and hence the production of polarized radiation. This picture is compatible with the configuration of Type Ia SNe in which Ca II-rich matter is illuminated by a central emission source. In this case, the radiation field is primarily radial and hence naturally anisotropic, and the photon pumping is intrinsically anisotropic. Under the framework of atomic alignment, the spatial distribution of Ca II cannot be inferred from its polarization. The photons are polarized through the interaction between optical pumping by an anisotropic radiation field and the ambient magnetic field, so the polarization mechanism will be in effect regardless of the spatial distribution of Ca II. This is totally different from the photosphere-blocking mechanism.

Particularly in the later stages of the expansion of a Type Ia SN, the ejecta become thin enough that the impact of collisions diminishes. In the case of Ca II, the photoexcitation from the ground state $^2S_{1/2}$ is dominated by the two E1 transitions of the Ca II H and K lines and followed by the cascade to the two metastable states $^2D_{3/2,5/2}$. As proposed by Yan & Lazarian (2006), the metastable states of Ca II NIR3 can be aligned in an anisotropic radiation field and magnetically realigned in the same fashion as their ground states. This happens to some atomic species because their metastable states are also long-lived, which makes them act similarly to the ground states and become sensitive to a weak magnetic field.

Assuming a blackbody radiation field of 5000 K, the photoexcitation rate from the ground state of Ca II NIR3 gives a photoexcitation rate of $\sim 2 \times 10^4 \text{ s}^{-1}$ (Yan & Lazarian 2006). This corresponds to the inverse of the lifetime of the metastable states, which in turn yields a low magnetic sensitivity of $\sim 1 \text{ mG}$ for the Ca II NIR3 (Carlin et al. 2013). In other words, the polarization of the Ca II NIR3 line potentially traces the component of the local magnetic field in the plane of the sky when the magnetic field is stronger than $\sim 1 \text{ mG}$. Based on the optical pumping from the ground state, particularly, we estimated the maximum degree of polarization for Ca II NIR3 reached in the ideal alignment case, with a beam of radiation and a local magnetic field aligned with it. Without counting the effect of collisions between atoms, the maximum degree of polarization for 8500.36 \AA ($2D_{3/2} > 2P_{3/2}$), 8544.44 \AA ($2D_{5/2} > 2P_{3/2}$), and 8664.52 \AA ($2D_{3/2} > 2P_{1/2}$) can reach 10.8%, 8.9%, and 12.5%, respectively. The highest polarization is higher compared to that in Ti II lines, $\sim 7\%$ for the two aligned metastable ($2D_{3/2,5/2}$) to the upper ($2P_{1/2,3/2}^O$) states, which exhibits similar but more complicated transitional structures compared to Ca II NIR3 (see, e.g., Table 3 of Yan & Lazarian 2012). A more detailed discussion of the Ca II NIR3 polarization computed based on the ground-state alignment theory will be presented in future work (H. Yan et al., in preparation).

Since all three components of the Ca II NIR3 triplet are magnetically alignable and can be individually polarized, the large width of the polarized feature on day +79 (see Figures 5, 6, and 9) is in agreement with the proposed atomic alignment mechanism. The polarization profile and peak level at this late time differ substantially from those around peak luminosity

(see Figures 2–3), when the line polarization was mainly due to an uneven obscuration of the photosphere by the line opacity. If the late-time polarization is indeed caused by atomic alignment in a weak magnetic field, the shape of the polarization profile may depend on (i) the anisotropy of the pumping radiation field, (ii) the ambient magnetic field, and (iii) the velocity field that affects the Ca opacity. The modeling of the Ca II NIR3 polarization profile is beyond the scope of this paper.

For atomic species to be aligned, the angular momentum of their ground state should be nonzero. For example, Ca II H and K, which is induced via the transition from the ground state to the upper state (i.e., $2S_{1/2} \rightarrow 2P_{1/2,3/2}^O$), is not alignable by this magnetic mechanism since the total angular momentum of the ground state is $J = 0$, which does not allow uneven occupation of ground-state angular momenta. Therefore, the Ca II H and K absorption would not be polarized by the same effect. However, although the uncertainty in the Stokes parameters becomes larger near the blue end of the spectral coverage, a similar evolution of increasing late-time Ca II polarization is also seen in the Ca II H and K lines. In Figures 4 and 5, we present the observed polarization position angles across both the Ca II H and K and Ca II NIR3 for SN 2021rhu after correcting for the ISP. At day +79, the two position angles exhibit significant differences, suggesting that the polarization mechanisms of the two Ca II lines are intrinsically different. In the case of uneven photosphere obscuration, the two features would be expected to exhibit similar polarization position angles, since both lines are likely to originate from the same Ca II opacity distribution.

5. Summary

Compared to the time around peak luminosity, we found a strong growth of the Ca II polarization observed in the Type Ia SN 2021rhu on days +36 and +79. The continuum polarization remained low at day +79 in spite of the drastic increase in polarization of Ca II NIR3; this is consistent with the low level measured for the continuum polarization at early phases when the photosphere has not yet receded into deep layers. We consider the possibility of line polarization due to partial blocking of the underlying photosphere by Ca-rich material, as well as an alternative explanation that Ca II NIR3 might be polarized through the alignment of the atoms with respect to an ambient weak magnetic field in an anisotropic radiation field. Detailed modeling of the late-time polarization of Ca II features by magnetic alignment should consider (1) the geometric distribution of the Ca II opacities, (2) the shape and degree of anisotropy of the induced radiation field, and (3) the strength and geometry of the magnetic field. Note that the radiation field above the photosphere is intrinsically anisotropic, and the majority of the photon pumping will happen along the radial directions. Such an anisotropic incident flux can induce an unequal population distribution over the magnetic sublevels. Without the flux anisotropy, the alignment of atomic angular momentum will not happen, and no polarization will be produced.

Assuming that SN 2021rhu is not a singular case, we briefly outline the open questions raised by the polarimetry of SN 2021rhu at late phases.

(i) Is the large Ca II NIR3 polarization observed on day +79 best explained by photospheric blocking or optical pumping effects or their combination, or is another process needed?

(ii) Do different explosion mechanisms predict specific late-time continuum and line polarization properties that can be used for diagnostic purposes?

(iii) Can the magnitude and geometry of the magnetic field be determined from the late-time Ca II NIR3 polarization profile?

(iv) Can the multicomponent polarization profiles of Si II λ 6355 and Ca II NIR3 and their evolution lay the foundation for an overarching consistent model?

During the rapid expansion of the ejecta, any preexisting magnetic field will be frozen in the ejecta and weaken as they expand. Evidence for high initial magnetic fields (in excess of 10^6 G at the surface of the progenitor WD) has been reported from infrared line profiles and light curves of Type Ia SNe (see, e.g., Penney & Hoefflich 2014; Hristov et al. 2021). The exact nature of the initial magnetic field of the WD and its evolution to late SN phases may be of great importance for the understanding of Type Ia SNe. Due to the rapid evolution of the SN ejecta, the radiation field may become sufficiently diluted and anisotropic, matching the conditions necessary for an effective atomic alignment for a wide range of atomic species and transitions. A rise of polarized atomic lines is expected at this epoch. Perhaps this mechanism is already at work in the observed polarization of Si II and Ca II lines even around maximum brightness.

This is a new area worth pursuing both theoretically and observationally in future studies. With a comprehensive understanding of the mechanism(s), the Ca II polarization may provide a measure in the ejecta of the magnetic field inherited from the progenitor. This would be a valuable new diagnostic of Type Ia SN explosion models. Future spectropolarimetry of Type Ia SNe extending to late phases is also essential to search for any systematics, to explain the polarization mechanism, to discriminate between orientation and intrinsic diversity, and to further understand the radiation distribution within the core.

We thank the anonymous referee for the careful scrutiny, which resulted in quite a few helpful suggestions that improved the quality of the manuscript. We are grateful to the European Organisation for Astronomical Research in the Southern Hemisphere (ESO) for the generous allocation of observing time. The polarimetry studies in this work are based on observations made with the VLT at ESO's La Silla Paranal Observatory under program ID 105.20AU. We especially thank the staff at Paranal for their proficient and highly motivated support of this project in service mode. The high-resolution spectra presented herein were obtained at the W. M. Keck Observatory, which is operated as a scientific partnership among the California Institute of Technology, the University of California, and the National Aeronautics and Space Administration (NASA). The Observatory was made possible by the generous financial support of the W. M. Keck Foundation. The authors wish to recognize and acknowledge the very significant cultural role and reverence that the summit of Maunakea has always had within the indigenous Hawaiian community. We are most fortunate to have the opportunity to conduct observations from this mountain.

PyRAF, PyFITS, and STSCI_PYTHON are products of the Space Telescope Science Institute, which is operated by AURA for NASA. STScI is operated by the Association of Universities for Research in Astronomy, Inc., under NASA contract NAS5-26555. This research has made use of NASA's Astrophysics Data System Bibliographic Services; the SIMBAD database, operated at CDS, Strasbourg, France; and the

NASA/IPAC Extragalactic Database (NED), which is operated by the Jet Propulsion Laboratory, California Institute of Technology, under contract with NASA.

The research of Y.Y. is supported through a Bengier-Winslow-Robertson Fellowship. M.B. acknowledges support from the Swedish Research Council (Reg. No. 2020-03330). A.V.F.'s group at U.C. Berkeley acknowledges generous support from the Miller Institute for Basic Research in Science (where A.V.F. was a Miller Senior Fellow), Sunil Nagaraj, Landon Noll, Gary and Cynthia Bengier, Clark and Sharon Winslow, Sanford Robertson, and many additional donors. L.G. acknowledges financial support from the Spanish Ministerio de Ciencia e Innovación (MCIN), the Agencia Estatal de Investigación (AEI) 10.13039/501100011033, and the European Social Fund (ESF) "Investing in your future" under the 2019 Ramón y Cajal program RYC2019-027683-I and the PID2020-115253GA-I00 HOSTFLOWS project, from Centro Superior de Investigaciones Científicas (CSIC) under the PIE project 20215AT016, and the program Unidad de Excelencia María de Maeztu CEX2020-001058-M. P.H. acknowledges the support from the NSF project "Signatures of Type Ia Supernovae, New Physics, and Cosmology," grant AST-1715133. The supernova research by L.W. is supported by NSF award AST-1817099. M.R. is supported by the National Science Foundation Graduate Research Fellowship Program under grant DGE-1752134. J.C.W. and J.V. are supported by NSF grant AST-1813825. The research of J.M. is supported through a Royal Society University Research Fellowship.

Facilities: VLT(FORS2), Keck:I (HIRES).

Software: IRAF (Tody 1986, 1993).

ORCID iDs

Yi Yang (杨轶)  <https://orcid.org/0000-0002-6535-8500>
 Huirong Yan  <https://orcid.org/0000-0003-2560-8066>
 Lifan Wang  <https://orcid.org/0000-0001-7092-9374>
 J. Craig Wheeler  <https://orcid.org/0000-0003-1349-6538>
 Dietrich Baade  <https://orcid.org/0000-0003-1637-9679>
 Howard Isaacson  <https://orcid.org/0000-0002-0531-1073>
 Aleksandar Cikota  <https://orcid.org/0000-0001-7101-9831>
 Justyn R. Maund  <https://orcid.org/0000-0003-0733-7215>
 Peter Hoefflich  <https://orcid.org/0000-0002-4338-6586>
 Ferdinando Patat  <https://orcid.org/0000-0002-0537-3573>
 Steven Giacalone  <https://orcid.org/0000-0002-8965-3969>
 Malena Rice  <https://orcid.org/0000-0002-7670-670X>
 Dakotah B. Tyler  <https://orcid.org/0000-0003-0298-4667>
 Divya Mishra  <https://orcid.org/0000-0001-5965-0997>
 Chris Ashall  <https://orcid.org/0000-0002-5221-7557>
 Thomas G. Brink  <https://orcid.org/0000-0001-5955-2502>
 Alexei V. Filippenko  <https://orcid.org/0000-0003-3460-0103>
 Llíus Galbany  <https://orcid.org/0000-0002-1296-6887>
 Kishore C. Patra  <https://orcid.org/0000-0002-1092-6806>
 Melissa Shahbandeh  <https://orcid.org/0000-0002-9301-5302>
 Sergiy S. Vasylyev  <https://orcid.org/0000-0002-4951-8762>
 Jozsef Vinkó  <https://orcid.org/0000-0001-8764-7832>

References

- Alsabti, A. W., & Murdin, P. 2017, *Handbook of Supernovae* (Cham: Springer)
- Anderson, J. 2018, EUROPEAN SOUTHERN OBSERVATORY, Doc. No. VLT-MAN-ESO,13100, http://www.eso.org/sci/facilities/paranal/instruments/fors/doc/VLT-MAN-ESO-13100-1543_P01.pdf
- Appenzeller, I., Fricke, K., Fürtig, W., et al. 1998, *Msngr*, 94, 1

- Atapin, K., Dodin, A., Tatarnikov, A., et al. 2021, Transient Name Server Classification Report [2021-2286](#)
- Bellm, E. C., Kulkarni, S. R., Graham, M. J., et al. 2019, *PASP*, **131**, 018002
- Black, C. S., Fesen, R. A., & Parrent, J. T. 2016, *MNRAS*, **462**, 649
- Blondin, S., Prieto, J. L., Patat, F., et al. 2009, *ApJ*, **693**, 207
- Boos, S. J., Townsley, D. M., Shen, K. J., Caldwell, S., & Miles, B. J. 2021, *ApJ*, **919**, 126
- Bravo, E., & García-Senz, D. 2009, *ApJ*, **695**, 1244
- Bravo, E., García-Senz, D., Cabezón, R. M., & Domínguez, I. 2009, *ApJ*, **695**, 1257
- Bulla, M., Sim, S. A., Kromer, M., et al. 2016a, *MNRAS*, **462**, 1039
- Bulla, M., Sim, S. A., Pakmor, R., et al. 2016b, *MNRAS*, **455**, 1060
- Cardelli, J. A., Clayton, G. C., & Mathis, J. S. 1989, *ApJ*, **345**, 245
- Carlin, E. S., Asensio Ramos, A., & Trujillo Bueno, J. 2013, *ApJ*, **764**, 40
- Cikota, A., Patat, F., Cikota, S., & Faran, T. 2017, *MNRAS*, **464**, 4146
- Cikota, A., Patat, F., Wang, L., et al. 2019, *MNRAS*, **490**, 578
- Cox, N. L. J., & Patat, F. 2014, *A&A*, **565**, A61
- Dhawan, S., Goobar, A., Johansson, J., et al. 2022, *ApJ*, **934**, 185
- Dong, S., Katz, B., Kushnir, D., & Prieto, J. L. 2015, *MNRAS*, **454**, L61
- Draine, B. T. 2003, *ARAA*, **41**, 241
- Fink, M., Röpke, F. K., Hillebrandt, W., et al. 2010, *A&A*, **514**, A53
- Graham, M. J., Kulkarni, S. R., Bellm, E. C., et al. 2019, *PASP*, **131**, 078001
- Graham, M. L., Valenti, S., Fulton, B. J., et al. 2015, *ApJ*, **801**, 136
- Hanle, W. 1924, *ZPhy*, **30**, 93
- Happer, W. 1972, *RvMP*, **44**, 169
- Höflich, P. 1991, *A&A*, **246**, 481
- Höflich, P., Khokhlov, A., Wheeler, J. C., et al. 1996, *ApJL*, **472**, L81
- Hough, J. H., Bailey, J. A., Rouse, M. F., & Whittet, D. C. B. 1987, *MNRAS*, **227**, 1P
- Howard, A. W., Johnson, J. A., Marcy, G. W., et al. 2010, *ApJ*, **721**, 1467
- Howell, D. A., Höflich, P., Wang, L., & Wheeler, J. C. 2001, *ApJ*, **556**, 302
- Hristov, B., Höflich, P., & Collins, D. C. 2021, *ApJ*, **923**, 210
- Iben, I., Jr., & Tutukov, A. V. 1984, *ApJs*, **54**, 335
- Ignace, R., Nordsieck, K. H., & Cassinelli, J. P. 1997, *ApJ*, **486**, 550
- Jordan, G. C. I., Fisher, R. T., Townsley, D. M., et al. 2008, *ApJ*, **681**, 1448
- Jordan, G. C. I., Graziani, C., Fisher, R. T., et al. 2012, *ApJ*, **759**, 53
- Kasen, D., Nugent, P., Wang, L., et al. 2003, *ApJ*, **593**, 788
- Kawabata, K. S., Akitaya, H., Yamanaka, M., et al. 2014, *ApJL*, **795**, L4
- Khokhlov, A., Mueller, E., & Höflich, P. 1993, *A&A*, **270**, 223
- Khokhlov, A. M. 1991a, *A&A*, **245**, 114
- Khokhlov, A. M. 1991b, *A&A*, **245**, L25
- Landolfi, M., & Landi Degl'Innocenti, E. 1986, *A&A*, **167**, 200
- Maund, J. R., Wheeler, J. C., Patat, F., et al. 2007, *MNRAS*, **381**, 201
- Maund, J. R., Wheeler, J. C., Wang, L., et al. 2010, *ApJ*, **722**, 1162
- Munari, U., & Zwitter, T. 1997, *A&A*, **318**, 269
- Munoz-Arancibia, A., Mourao, A., Forster, F., et al. 2021, Transient Name Server Discovery Report [2021-2265](#)
- Pakmor, R., Kromer, M., Röpke, F. K., et al. 2010, *Natur*, **463**, 61
- Pakmor, R., Kromer, M., Taubenberger, S., et al. 2012, *ApJL*, **747**, L10
- Patat, F., Baade, D., Höflich, P., et al. 2009, *A&A*, **508**, 229
- Patat, F., Chandra, P., Chevalier, R., et al. 2007, *Sci*, **317**, 924
- Patat, F., Maund, J. R., Benetti, S., et al. 2010, *A&A*, **510**, A108
- Patat, F., & Romaniello, M. 2006, *PASP*, **118**, 146
- Patat, F., Taubenberger, S., Cox, N. L. J., et al. 2015, *A&A*, **577**, A53
- Penney, R., & Höflich, P. 2014, *ApJ*, **795**, 84
- Phillips, M. M., Simon, J. D., Morrell, N., et al. 2013, *ApJ*, **779**, 38
- Plewa, T., Calder, A. C., & Lamb, D. Q. 2004, *ApJL*, **612**, L37
- Porter, A. L., Leising, M. D., Williams, G. G., et al. 2016, *ApJ*, **828**, 24
- Poznanski, D., Prochaska, J. X., & Bloom, J. S. 2012, *MNRAS*, **426**, 1465
- Schlafly, E. F., & Finkbeiner, D. P. 2011, *ApJ*, **737**, 103
- Seitenzahl, I. R., Ciaraldi-Schoolmann, F., Röpke, F. K., et al. 2013, *MNRAS*, **429**, 1156
- Serkowski, K., Mathewson, D. S., & Ford, V. L. 1975, *ApJ*, **196**, 261
- Shen, K. J., Kasen, D., Weinberg, N. N., Bildsten, L., & Scannapieco, E. 2010, *ApJ*, **715**, 767
- Simon, J. D., Gal-Yam, A., Gnat, O., et al. 2009, *ApJ*, **702**, 1157
- Srivastav, S., Ninan, J. P., Kumar, B., et al. 2016, *MNRAS*, **457**, 1000
- Sternberg, A., Gal-Yam, A., Simon, J. D., et al. 2011, *Sci*, **333**, 856
- Taam, R. E. 1980, *ApJ*, **242**, 749
- Tody, D. 1986, *Proc. SPIE*, **627**, 733
- Tody, D. 1993, in ASP Conf. Ser. 52, Astronomical Data Analysis Software and Systems II, ed. R. J. Hanisch, R. J. V. Brissenden, & J. Barnes (San Francisco, CA: ASP), 173
- van Driel, W., Butcher, Z., Schneider, S., et al. 2016, *A&A*, **595**, A118
- Vogt, S. S., Allen, S. L., Bigelow, B. C., et al. 1994, *Proc. SPIE*, **2198**, 362
- Wang, L., Baade, D., Höflich, P., et al. 2003, *ApJ*, **591**, 1110
- Wang, L., Baade, D., Höflich, P., et al. 2006, *ApJ*, **653**, 490
- Wang, L., Howell, D. A., Höflich, P., & Wheeler, J. C. 2001, *ApJ*, **550**, 1030
- Wang, L., & Wheeler, J. C. 1996, *ApJL*, **462**, L27
- Wang, L., & Wheeler, J. C. 2008, *ARAA*, **46**, 433
- Wang, L., Wheeler, J. C., & Höflich, P. 1997, *ApJL*, **476**, L27
- Wang, X., Chen, J., Wang, L., et al. 2019, *ApJ*, **882**, 120
- Webbink, R. F. 1984, *ApJ*, **277**, 355
- Whittet, D. C. B., Martin, P. G., Hough, J. H., et al. 1992, *ApJ*, **386**, 562
- Wright, J. T., & Eastman, J. D. 2014, *PASP*, **126**, 838
- Yan, H., & Lazarian, A. 2006, *ApJ*, **653**, 1292
- Yan, H., & Lazarian, A. 2008, *ApJ*, **677**, 1401
- Yan, H., & Lazarian, A. 2012, *JQSR*, **113**, 1409
- Yang, Y., Höflich, P., Baade, D., et al. 2020, *ApJ*, **902**, 46
- Yang, Y., Wang, L., Baade, D., et al. 2018, *ApJ*, **854**, 55